Expeditious Electrochemical Synthesis of Mesoporous Chalcogenide Flakes: Mesoporous Cu_2Se as a Potential High-Rate Anode for Sodium-Ion Battery

Tomota Nagaura, Jinliang Li*, Joseph F. S. Fernando, Aditya Ashok, Azhar Alowasheeir, Ashok Kumar Nanjundan, Sukho Lee, Dmitri V. Golberg, Jongbeom Na* and Yusuke Yamauchi*

Tomota Nagaura, Aditya Ashok, Jongbeom Na, Yusuke Yamauchi
Australian Institute for Bioengineering and Nanotechnology (AIBN), The University of Queensland, Brisbane, QLD 4072, Australia
Email: y.yamauchi@uq.edu.au

Jinliang Li
Siyuan Laboratory, Guangzhou Key Laboratory of Vacuum Coating Technologies and New Energy Materials, Guangdong Provincial Engineering Technology Research Center of Vacuum Coating Technologies and New Materials, Department of Physics, Jinan University, Guangzhou, Guangdong 510632, China
Email: lijinliang@email.jnu.edu.cn

Joseph F.S. Fernando, Dmitri V. Golberg
Centre for Materials Science and School of Chemistry and Physics, Queensland University of Technology (QUT), 2 George Str., Brisbane, QLD 4000, Australia

Alowasheeir Azhar, Yusuke Yamauchi
JST-ERATO Yamauchi Materials Space-Tectonics Project and International Center for Materials Nanoarchitectonics (WPI-MANA), National Institute for Materials Science (NIMS), 1-1 Namiki, Tsukuba, Ibaraki 305-0044, Japan

Ashok Kumar Nanjundan, Yusuke Yamauchi
School of Chemical Engineering, The University of Queensland, Brisbane, QLD 4072, Australia

Sukho Lee, Jongbeom Na
Research and Development (R&D) Division, Green Energy Institute, Mokpo, Jeollanamdo 58656, Republic of Korea

Email: j.na@gei.re.kr

Keywords: Block copolymers, Electrochemical deposition, Mesoporous semiconductors, Self-assembly, Na-ion batteries

Nanostructured copper selenide attracts much interest as it shows outstanding performance as thermoelectric, photo-thermal, and optical material. Mesoporous structure is also promising morphology to obtain better performance for electrochemical and catalytic applications, thanks to its high surface area. We propose a simple one-step electrochemical method for mesoporous chalcogenides synthesis. The synthesized copper selenide (Cu_2Se) material has two types of mesopores (9 and 18 nm in diameter) which are uniformly distributed inside the flakes. We also implement these materials for NIBs anode as a proof of concept. The electrode employing the mesoporous Cu_2Se exhibits superior and more stable specific capacity as a NIB's anode compared to the non-porous samples. The electrode also exhibits excellent rate tolerance at each current density, from 100 to 1,000 mA g^{-1}. We suggest that the mesoporous structure is advantageous for the insertion of Na ions inside the flakes. Electrochemical analysis indicates that the mesoporous electrode possesses more prominent diffusion-controlled kinetics during the sodiation-desodiation process, which contributes to the improvement of Na-ion storage performance.

1. Introduction

Copper chalcogenide semiconductors are exceedingly fascinating materials in research and industrial fields as they have versatile phases and may compose of mixed phases with other elements, enabling a wide range of bandgaps for light-driven applications and excellent functional properties in chemistry and physics fields.[1-4] Due to the low cost and the relative abundance, copper selenide has a high potential to be applied industrially and in research. It is widely applicable in optics, catalysis, and bioengineering fields. It may also conveniently serve as a precursor material for copper indium diselenide (CIS) or copper indium gallium diselenide (CIGS) solar cells,[5] thermo-electronics,[6] and photothermal materials as a cancer aid.[2,7] Copper selenide can be formed in many phases, such as Cu_2Se, CuSe, Cu_3Se_2, *etc.*, and interestingly, the energy bandgap is compositionally dependent.[1,7,8] Especially, Cu_2Se forms two phases at room temperature, namely, α-phase and β-phase.[8-10] The β-phase exhibits high conductivity, thanks to its unique crystal nature.[11,12] Cu atoms can exist at different locations, resulting in three types of crystal structures, namely, monoclinic, tetragonal, and cubic.[13-15]

Copper selenide materials are promising for rechargeable batteries, such as alkali metal-ion batteries.[16-18] Among the alkali metal-ion batteries, sodium (Na) ion battery (NIB) is currently expected as a decent alternative to Li-ion batteries (LIBs), because Na is nontoxic and more abundant in the Earth's crust compared to Li.[19] Due to high demand for large-scale rechargeable batteries, especially in electric cars and battery storage in houses, the production

cost and the abundance must first be considered. Current research in NIBs applications has reported significant progress in battery capacity utilizing common materials. N-doped C@$Zn_3B_2O_6$ shows around 300 mAh g^{-1} capacity at 100 mA g^{-1} in the initial several 10 cycles.[20] $KMeO_2$ (Me = transition metal) and micro-structured MnO_2 are other decent materials for a NIBs anode, showing around 100 mAh g^{-1} capacity at the same current density.[21-23] Cu_2Se in the β-phase has also a high potential for an anode as it shows reversible transformations to Na_2Se through different intermediate compositions during the charge/discharge processes, such as $Na_yCu_{2-x}Se$ and NaCuSe/Cu, and has a high theoretical specific capacity for NIBs.[16] Several reports have proposed the synthesis of nanoscale copper chalcogenides, such as nanoparticles,[24] nanotubes,[25] *etc*. Meanwhile, those have several disadvantages, such as severe aggregation and/or requiring assistance for self-standing. In addition, there have been very few reports on mesoporous chalcogenides. And no a single report on synthesizing highly uniform mesoporous Cu_2Se is available. This would be the next challenge in the materials field.

The solvothermal process is a potential process to induce mesopores *via* nano-crystallization.[16] A mesoporous Cu_2Se shows high reversibility and keeps high capacity during long-term cycles, resulting in up to 96 % utilization of its theoretical capacity and 88 % retention after 2,000 cycles at 5 A g^{-1}. Therefore, such a mesoporous architecture would be one of the most promising morphologies for a high-performance anode. However, the induced mesopores are randomly dispersed and their pore sizes are non-uniform, due to the standard nano-crystallization process. Another potential method is inducing mesopores using liquid crystals during electrochemical synthesis. Uniform mesopores of CdTe have indeed been reported by employing viscous liquid crystals, but the pore size has been theoretically limited to 10 nm due to the molecular sizes of templates.[26] Also, highly viscous electrolytes would also make the synthesis difficult, and thus there have been no reports on the uniformly sized mesoporous Cu_2Se.

In recent years, our group has demonstrated many types of mesoporous metals and alloys utilizing block copolymer micelles.[27-29] Very recently, we have also applied this method to chalcogenide materials.[30] This enables architecting the well-designed mesoporous structures using block copolymers and controlling the compositions *via* a simple process. The size-tunable pores at nanoscale can uniformly and densely be dispersed, thus enhancing the electrochemically active surface area and the intrinsic material performance including electrochemical activities.[29-32] Compared to films adhered to substrates, powdery samples are

indispensable for many practical applications, including rechargeable batteries. Thus further development of this direction is required.

Therefore herein, we demonstrate the electrochemical synthesis of mesoporous Cu_2Se flakes through a simple one-step method. This method does not require any expensive and complicated equipment as it simply utilizes an electrodeposition process. It also enables expeditious material growth compared to other sluggish processes, *i.e.* solvothermal or chemical/physical vapor deposition processes. Although the electrochemical method essentially forms a thin film onto a conductive substrate, it can be widely applicable to any other shapes in addition to the flake shape, which is also in high demand for alkaline metal-ion batteries.[33,34] The resulting samples have self-standing numerous mesopores homogeneously dispersed within entire flakes. They also exhibit large electrochemically active surface area and high performance in NIB applications. The specific capacities of the mesoporous electrode are 374, 327, 311, and 295 mAh g^{-1} at each current density of 100, 200, 500, and 1,000 mA g^{-1}, respectively. Those performances are comparable with other current high-performance Cu_2Se anodes.[16,35-37] For a Na-ion full battery system, several potential cathode materials have been recently reported, such as $Na_3V_2(PO_4)_2O_2F$ and pre-sodiated reduced graphene oxide (rGO), showing excellent full battery performance with respect to specific capacity over long cycles.[38,39] $Na_3V_2(PO_4)_2F_3$@rGO has been also utilized with a Cu_2Se anode, exhibiting reasonable specific capacity, such as 100-200 mAh g^{-1} at 0.1-2 A g^{-1}.[37] Those materials would be potentially appropriate for the anode in the regarded mesoporous Cu_2Se battery in the future.

2. Results and Discussions

The one-step process enables electrochemical fabrication of mesoporous Cu_2Se films onto a conductive substrate, as shown in Figure 1a. Cu_2Se is electrodeposited on a conductive substrate in the solution containing micelles. This concept is based on our previous research, and two types of pore sizes, *i.e.* 9 nm and 18 nm pores, are achieved by using a different type of block copolymers.[29,30] Cyclic voltammetry (CV) was conducted to investigate electrochemical reactions in the Cu-Se solution (Figure S1a). Cu_2Se films have been deposited at a -0.1 V potential (*vs.* SHE) in each solution (Table S1), showing a stable current during the synthesis (Figure S1b). Although Cu_2Se is one of the chalcogenide semiconductors, it has high conductivity and is available for stable electrochemical film growth. The long-term film growth onto indium tin-doped oxide (ITO) substrate makes it possible the Cu_2Se flakes collection from the substrate because of their low adhesion to it. The films are easily collected after electrodeposition, although

a few parts still remain on the substrate (Movie S1). The PS cores are removed by rinsing in pure THF solution at 60 ˚C. The obtained powders were applied to NIB through a device assembly process.

When an Au/Si substrate is used, relatively good adhesion to Cu_2Se (Figure S2) is confirmed. The grown film shows a blueish glossy surface (Figure S2d). On the other hand, the transparent films reveal an orange color after electrodeposition onto the ITO substrate (Figure 1b) and possess a varying energy bandgap for each sample before the heat treatment (Figure S3). The intrinsic energy bandgap of *β*-phase is 2.1-2.3 eV.[9,40] Meanwhile, other related material such as Cu_2Se_3 shows a higher energy band gap, approximately 2.7-2.9 eV.[40] The present energy bandgaps are aligned to the 2.13-2.15 eV values (Figure S3) after heat treatment at 145 ˚C under an inert N_2 atmosphere, confirming that all the obtained phases belong to the *β*-phase.[40]

Surface morphologies of Cu_2Se films reveal a uniform mesoporous structure in contrast to the non-porous film which shows a specific fibrous structure (Figure S2a-c). The obtained film compositions were analyzed by energy-dispersive X-ray spectroscopy (EDS). It is revealed that the films have a nearly stoichiometric composition of Cu_2Se (with a deviation of only 1.5-1.6 % for all the samples (Figure S2e)). The pore sizes are calculated to be 9.2 nm and 18.1 nm, respectively (Figure S4a). These mesopores are created by polystyrene cores of comparable diameters, whose size can be controlled by a molecular weight of the block copolymer.[29] The validation coefficients of pore sizes are 15 % and 18 % in 9-nm and 18-nm pore samples, respectively. The pore-to-pore distances are 19.8 nm and 30.0 nm in 9-nm and 18-nm pore samples (with 14 % and 13 % validation coefficients, respectively (Figure S4b)). Small-angle X-ray scattering profiles also confirm that each pore-to-pore distances are around 20.9 nm and 30.5 nm (Figure S5), which are in accord with the results in Figure S4b.

According to the analysis using field emission scanning electron microscopy (FE-SEM), Cu_2Se film cross-sections retain the specific features during the film growth (Figure S6). Furthermore, a smooth surface is maintained during the film growth (up to 700 s) for all the samples. The cross-sections of the non-porous sample reveal relatively larger hollow interiors which are formed because of the intrinsic fibrous structure (Figure S2c). The film growth rates were calculated based on the thickness of each film, as shown in Figure S7. The film thicknesses are linearly increased with the applied electrodeposition times. The growth rates are 0.45 nm s^{-1}, 0.43 nm s^{-1}, and 0.61 nm s^{-1} in 9-nm pore, 18-nm pore, and non-porous samples, respectively (Figure S7).

Electrochemical surface areas (ECSAs) were evaluated using CV analysis. The values are 2.5 mF cm^{-2} and 0.72 mF cm^{-2} for 9-nm and 18-nm pore films, respectively, with a 350 nm film thickness on the Au/Si substrate (Figure S8). In this measurement, the capacitances were measured by sweeping around the open circuit potential to analyze an electrical double layer. The calculated values for 9-nm and 18-nm pore films (2.5 mF cm^{-2} and 0.72 mF cm^{-2}) are 58 and 17 times higher than that for the non-porous film (0.043 mF cm^{-2}). Such huge increase is valuable for catalytic or electrochemical applications. The chemical surface states were further investigated by XPS analysis (Figure S9). Clear peaks of Cu ($2p_{3/2}$ and $2p_{1/2}$) and Se ($3d_{5/2}$ and $3d_{3/2}$) indicate that the surfaces are characteristics of pure copper selenide. Even though the materials are exposed to the air before XPS analysis, only weak oxidation peaks of Cu (936 eV) and Se (59 eV) are detected, implying that the mesoporous Cu_2Se well tolerates the oxidation.[41]

The surfaces and cross-sections of the flakes collected from the ITO substrate were then analyzed by FE-SEM in detail (Figure 2). After electrochemical deposition over a long time, the films reveal a micrometer-scale thickness (Figure 2b). The cross-sectional images indicate that the internal structures are formed by a mesoporous network (Figure 2d, f), similar to the films on the Au/Si substrate (Figure S2a, b). All the samples (9-nm, 18-nm and non-porous samples) show a similar fibrous texture on the flake surface (Figure 2c, e, g). The non-porous flakes seemingly have micrometer-scale hollow structures inside the film, resulting from the continuous growth of their fibrous morphology (Figure 2g, h). Their fibrous nature becomes more obvious compared to the films grown over less than 700 s (Figure S6).

The sample flakes were then analyzed by X-ray powder diffraction (XRD) and high-resolution transmission electron microscopy (HRTEM) (Figure 3). According to XRD analysis, the strong peaks of β-phase Cu_2Se are obvious. The grain size was calculated by the Scherrer equation using the strongest peaks at 46.7°. The calculation gave the numbers of 54 nm, 61 nm, and 99 nm for 9-nm, 18-nm pore and non-porous samples, respectively (Figure 3a). The grain sizes are larger than the thickness of pore walls, indicating that crystallinity is coherently extended across several mesopores (Figure 3b, c). The HRTEM image of the selected fragment indicates a pore size of around 20 nm in diameter, as indicated by an arrow (Figure 3c). The diffraction pattern is a characteristic of a polycrystal with 0.33 nm, 0.21 nm, and 0.17 nm lattice distances, natural to (111), (220), and (311) planes, respectively (Figure 3d), which agrees with the

XRD results (Figure 3a). The EDS elemental mapping data confirms the uniform distribution of Cu and Se atoms throughout the structures (Figure 3e).

The performance of NIBs was electrochemically evaluated using non-porous and 18-nm pore Cu_2Se flakes. The initial CV curves of non-porous and 18-nm pore samples were first analyzed. Both the electrodes exhibit some irreversible peaks during the initial discharge stage (Figure S10), indicating formation of a thin solid electrolyte interface (SEI) layer.[42,43] Furthermore, galvanostatic charge-discharge curves of non-porous and 18-nm pore samples reveal that both electrodes present a similar specific capacity for Na-ion storage (Figure 4a). After the desodiation process, however, the 18-nm pore sample shows better reversibility than that of non-porous one, suggesting that the mesoporous Cu_2Se is a better fit for a reversible migration during the sodiation-desodiation process. Figure 4b shows the cycling performance (up to the 50^{th} cycle) of both samples. One interesting point is that the specific capacity of the non-porous sample rapidly fades over the initial few cycles, which should be due to the low charge transfer kinetics in non-porous materials, resulting in a poor Na-ion diffusion at this stage.[44,45] Then, after around the 10^{th} cycle, a distinct increase in specific capacity is observed. This should be due to the optimization of electrolyte-derived surface layers under further cycling.[46,47] Some inactive sites of Cu_2Se can be excited, contributing to a further increase in specific capacity. At the 50^{th} cycle, the non-porous sample provides a high specific capacity of 293 mAh g^{-1} at 100 mA g^{-1}. Meanwhile, the 18-nm pore sample exhibits a discharge specific capacity of 323 mAh g^{-1} with a reversible specific capacity of 308 mAh g^{-1} at the 50^{th} cycle. The capacity of the 18-nm pore sample is a little higher than that of the non-porous sample. It should be noted that the 18-nm pore sample exhibits a very stable cycling performance in the initial stage, unlike the non-porous sample. The numerous mesopores allow Na-ions to be easily transferred inside the electrode material. Previous reports demonstrated that the original mesoporous structure remains even after the cycling tests, in which the mesopores can bare a volume change during the charge and discharge processes.[16,48,49] The similar situation is probably true in our experiments.

In addition, it is found that both the electrodes possess quite high Coulombic efficiencies during the sodiation-desodiation processes (Figure 4c). High initial Coulombic efficiency generally means high utilization of Na-ions in a full battery setup essential for NIBs. The 18-nm pore sample presents a high initial Coulombic efficiency of 95.4 %. This value is comparable with the most recent Cu_2Se and other chalcogenide materials tested in NIBs (in the range of 70-100 %).[16,50-57]

The rate performance was then investigated for further assessment of the electrochemical performance (Figure 4d). The non-porous sample delivers the reversible specific capacities of 388, 259, 238, and 239 mAh g^{-1} at 100, 200, 500, and 1,000 mA g^{-1}, respectively. On the other hand, the 18-nm pore sample presents an enhanced rate performance for Na-ion storage, showing the reversible specific capacities of 374, 327, 311, and 295 mAh g^{-1} at 100, 200, 500, and 1,000 mA g^{-1}, respectively. These capacities are above the Cu_2Se theoretical capacity of 260 mA g^{-1} because of the existing defects and surface adsorption which can contribute to additional capacity.[58] The higher capacities of the 18-nm sample than those of the non-porous sample are derived from the intensification of kinetic processes inside the mesopores. As shown in Figure 4b, although the capacity decrease of the non-porous sample is observed in the initial stage due to the low charge transfer kinetics, the 18-nm pore sample presents a lesser capacity decrease in the initial stage owing to the mesoporous structure. To confirm this conclusion, the electrochemical impedance spectroscopy tests of non-porous and 18-nm pore electrodes were carried out (Figure S11). It was found that the 18-nm pore sample better facilitates the charge transfer kinetics.

To further analyze the kinetic behavior of both non-porous and 18-nm pore electrodes, each CV was investigated at different scan rates (Figure 5a, b). Both samples have the same reaction processes during sodiation. The 18-nm pore sample evenly increases the current at a scan rate from 1.5 to 2.0 V, suggesting faster diffusion reactions in this region. For further investigation of the electrochemical behavior, the relationship between current (*i*) and scan rate (*v*) was calculated using the following equation[59,60]:

$$i = av^b \qquad (1)$$

It can be transformed into the following equation:

$$\log i = \log a + b \log v \qquad (2)$$

The *b* value is determined by a slope of the plot between current and scan rates. It is generally known that the *b* value shows ~0.5 number under the diffusion-controlled behavior, while it becomes around 1.0 when a capacitive behavior becomes in effect. Six redox peaks of the non-porous and 18-nm pore samples were selected for fitting to obtain the *b* values (Figure 5c, d). All the *b* values calculated from each peak are close to 1.0, manifesting that the capacitive behavior becomes dominant. To quantify the kinetic behavior, the capacitive contributions were also confirmed using the following equation[61,62]:

$$i(V) = k_1 v + k_2 v^{1/2} \qquad (3)$$

Then, the following equation can be obtained after conversion:

$$i(V)/v^{1/2} = k_1 v^{1/2} + k_2 \qquad (4)$$

The $k_1 v$ and $k_2 v^{1/2}$ terms are regarded to reflect the capacitive behavior and diffusion-controlled behavior, respectively. The non-porous sample shows 88 % capacitive behaviors at 1 mV s^{-1}, thus a slightly higher value than 86 % for the 18-nm pore sample. It means that the mesoporous electrode shows better diffusion-controlled behavior during the sodiation-desodiation processes. This contributes to the improvement of NIB specific capacity. Figures 5g-h comparatively show the capacitive and diffusion-controlled behaviors at different scan rates. More prominent diffusion-controlled behaviors can be obtained for the 18-nm pore sample, suggesting that numerous mesopores improve the redox reaction in the sodiation-desodiation processes.

3. Conclusion

Two types of mesoporous Cu_2Se flakes with different pore sizes (around 9 and 18 nm) have been synthesized *via* a simple electrochemical synthesis using a block copolymer followed by detaching the deposited films from an ITO substrate. Detailed structural analyses have confirmed that the resulting Cu_2Se material contains numerous mesopores. Such mesopores are uniformly distributed within the flakes, thereby creating a huge electrochemically active surface area. The mesoporous Cu_2Se shows high performance in NIB application. Both the mesoporous and non-porous samples reveal high reversible specific capacities of over 300 mAh g^{-1}. Our mesoporous electrode exhibits more stable performance, over 300 mAh g^{-1} in each cycle. The mesoporous architecture contributes to efficiently delivering Na-ions inside the electrode material. Through a careful investigation using the CV analyses at different scan rates, it has been revealed that the more prominent diffusion-controlled behavior contributes to the improvement of the sodiation-desodiation reactions in the mesoporous samples.

Supporting Information

Supporting Information is available from the Wiley Online Library or from the author.

Acknowledgements

The authors are grateful to the Australian Research Council (ARC) for funding in the frame of the ARC Laureate Project FL160100089 and the ARC Linkage Project (LP180100429). The authors also acknowledge the Fundamental Research Funds for the Central Universities (21621406) and Science and Technology Program of Guangzhou, China (202102020737,

201605030008). This work was in part performed at the Queensland node of the Australian National Fabrication Facility (ANFF-Q), a company established under the National Collaborative Research Infrastructure Strategy to provide nano- and microfabrication facilities for Australian researchers.

Received: ((will be filled in by the editorial staff))
Revised: ((will be filled in by the editorial staff))
Published online: ((will be filled in by the editorial staff))

References

[1] C. Coughlan, M. Ibanez, O. Dobrozhan, A. Singh, A. Cabot, K. M. Ryan, *Chem. Rev.* **2017**, *117*, 5865.

[2] S. Zhang, C. Sun, J. Zeng, Q. Sun, G. Wang, Y. Wang, Y. Wu, S. Dou, M. Gao, Z. Li, *Adv. Mater.* **2016**, *28*, 8927.

[3] D. Yang, Q. Zhu, C. Chen, H. Liu, Z. Liu, Z. Zhao, X. Zhang, S. Liu, B. Han, *Nat. Commun.* **2019**, *10*, 677.

[4] D. Byeon, R. Sobota, K. Delime-Codrin, S. Choi, K. Hirata, M. Adachi, M. Kiyama, T. Matsuura, Y. Yamamoto, M. Matsunami, T. Takeuchi, *Nat. Commun.* **2019**, *10*, 72.

[5] M. Kemell, M. Ritala, M. Leskela. *Crit. Rev. Solid State Mater. Sci.* **2005**, *30*, 1.

[6] Z. Lin, C. Hollar, J. S. Kang, A. Yin, Y. Wang, H. Y. Shiu, Y. Huang, Y. Hu, Y. Zhang, X. Duan, *Adv. Mater.* **2017**, *29*, 1606662.

[7] C. M. Hessel, V. P. Pattani, M. Rasch, M. G. Panthani, B. Koo, J. W. Tunnell, B. A. Korgel, *Nano Lett*. **2011**, *11*, 2560.

[8] S. C. Singh, H. Li, C. Yao, Z. Zhan, W. Yu, Z. Yu, C. Guo, *Nano Energy* **2018**, *51*, 774.

[9] V. M. Glazov, A. S. Pashinkin, V. A. Fedorov, *Inorg. Mater.* **2000**, *36*, 641.

[10] T. Godecke, T. Haalboom, F. Ernst. *Z. Met.kd.* **2000,** *91*, 622.

[11] D. Li, Z. Zheng, Y. Lei, S. Ge, Y. Zhang, Y. Zhang, K. W. Wong, F. Yang, W. M. Lau, *CrystEngComm* **2010**, *12*, 1856.

[12] J. Lee, Y. Gim, J. Yang, H. Jo, J. Han, H. Lee, D. H. Kim, W. Huh, J. H. Cho, M. S. Kang, *J. Phys. Chem.* C **2017**, *121*, 5436.

[13] E. J. D. Garba, R. L. Jacobs, *Physica B+C* **1986**, *138*, 253.

[14] H. Liu, X. Shi, F. Xu, L. Zhang, W. Zhang, L. Chen, Q. Li, C. Uher, T. Day, G. J. Snyder, *Nat. Mater*. **2012**, *11*, 422.

[15] B. Yu, W. Liu, S. Chen, H. Wang, H. Wang, G. Chen, Z. Ren, *Nano Energy* **2012**, *1*, 472.

[16] Y. Li, X. Sun, Z. Cheng, X. Xu, J. Pan, X. Yang, F. Tian, Y. Li, J. Yang, Y. Qian, *Energy Storage Mater*. **2019**, *22*, 275.

[17] J. L. Yue, Q. Sun, Z. W. Fu, *Chem. Commun.* **2013**, *49*, 5868.

[18] H. Lin, M. Li, X. Yang, D. Yu, Y. Zeng, C. Wang, G. Chen, F. Du, *Adv. Energy Mater.* **2019**, *9*, 1900323.

[19] H. Kim, H. Kim, Z. Ding, M. H. Lee, K. Lim, G. Yoon, K. Kang, *Adv. Energy Mater.* **2016**, *6*, 1600943.

[20] S. Wang, X. Zhang, *Adv. Mater.* **2019**, *31*, 1805432.

[21] S. Wang, T. Sun, S. Yuan, Y. Zhu, X. Zhang, J. Yan, Q. Jiang, *Mater. Horiz.* **2017**, *4*, 1122.

[22] S. Wang, Y. Zhu, J. Yan, X. Zhang, *J. Mater. Chem. A* **2018**, *6*, 13075.

[23] N. F. M. Yusoff, N. H. Idris, M. F. M. Din, S. R. Majid, N. A. Harun, M. M. Rahman, *Sci. Rep.* **2020**, *10*, 9207.

[24] W. Li, R. Zamani, P. R. Gil, B. Pelaz, M. Ibáñez, D. Cadavid, A. Shavel, R. A. Alvarez-Puebla, W. J. Parak, J. Arbiol, A. Cabot, *J. Am. Chem. Soc.* **2013**, *135*, 7098.

[25] S. Y. Zhang, C. X. Fang, Y. P. Tian, K. R. Zhu, B. K. Jin, Y. H. Shen, J. X. Yang, *Cryst. Growth Des.* **2006**, *6*, 2809.

[26] X. Li, I. S. Nandhakumar, T. Gabriel, G. S. Attard, M. L. Markham, D. C. Smith, J. J. Baumberg, K. Govender, P. O'Brien, D. Smyth-Boyle, *J. Mater. Chem.* **2006**, *16*, 3207.

[27] H. Wang, L. Wang, T. Sato, Y. Sakamoto, S. Tominaka, K. Miyasaka, N. Miyamoto, Y. Nemoto, O. Terasaki, Y. Yamauchi, *Chem. Mater.* **2012**, *24*, 1591.

[28] C. Li, Ö. Dag, T. D. Dao, T. Nagao, Y. Sakamoto, T. Kimura, O. Terasaki, Y. Yamauchi, *Nat. Commun.* **2015**, *6*, 6608.

[29] H. Lim, K. Kani, J. Henzie, T. Nagaura, A. S. Nugraha, M. Iqbal, Y. S. Ok, M. S. A. Hossain, Y. Bando, K. C. W. Wu, H. J. Kim, A. E. Rowan, J. Na, Y. Yamauchi, *Nat. Protoc.* **2020**, *15*, 2980.

[30] T. Nagaura, H.-P. Phan, V. Malgras, T.-A. Pham, H. Lim, A. Ashok, J. Kim, J. You, N.-T. Nguyen, J. Na, Y. Yamauchi, *Angew. Chem., Int. Ed.* **2021**, *60,* 9660.

[31] Y. Li, B. P. Bastakoti, V. Malgras, C. Li, J. Tang, J. H. Kim, Y. Yamauchi, *Angew. Chem., Int. Ed.*, **2015**, *54*, 11073.

[32] B. Jiang, C. Li, O. Dag, H. Abe, T. Takei, T. Imai, M. S. A. Hossain, M. T. Islam, K. Wood, J. Henzie, Y. Yamauchi, *Nat. Commun.* **2017**, *8*, 15581.

[33] Y. Zhu, X. Yang, D. Bao, X. Bie, T. Sun, S. Wang, Y. Jiang, X. Zhang, J. Yan, Q. Jiang, *Joule* **2018**, *2*, 736.

[34] H. Wang, W. Li, D. Liu, X. Feng, J. Wang, X. Yang, X. Zhang, Y. Zhu, Y. Zhang, *Adv. Mater.* **2017**, *29*, 1703012.

[35] Y. Xiao, X. Zhao, X. Wang, D. Su, S. Bai, W. Chen, S. Fang, L. Zhou, H.-M. Cheng, F. Li, *Adv. Energy Mater.* **2020**, *10,* 2000666.

[36] A. Molkenova, L. Khamkhash, A. Zhussupbekova, K. Zhussupbekov, S. Sarsenov, I. Taniguchi, I. V. Shvets, T. S. Atabaev, *Nanomaterials* **2020**, *10*, 1132.

[37] L. Shao, S. Wang, J. Qi, Z. Sun, X. Shi, Y. Shi, X. Lu, *Mater. Today Phys.* **2021**, *19*, 100422.

[38] G. Zheng, Q. Lin, J. Ma, J. Zhang, Y. He, X. Tang, F. Kang, W. Lv, Q. Yang, *InfoMat* **2021**, *3*, 1445.

[39] H. Liang, Z. Gu, X. Zhao, J. Guo, J. Yang, W. Li, B. Li, Z. Liu, W. Li, X. Wu, *Angew. Chem. Int. Ed*. **2021**, *60*, 26837.

[40] M. Lakshmi, K. Bindu, S. Bini, K. P. Vijayakumar, C. S. Kartha, T. Abe, Y. Kashiwaba, *Thin Solid Films*, **2001**, *386*, 127.

[41] J. F. Moulder, W. F. Stickle, P. E. Sobol, K. D. Bomben, *Handbook of X-ray Photoelectron Spectroscopy*, ed. J. Chastain (Perkin-Elmer Corp.) **1992**

[42] J. Xie, X. Li, H. Lai, Z. Zhao, J. Li, W. Zhang, W. Xie, Y. Liu, W. Mai, *Angew. Chem., Int. Ed.* **2019,** *58* 14740.

[43] S. Men, H. Zheng, D. Ma, X. Huang, X. Kang, *J. Energy Chem.* **2021**, *54*, 124.

[44] M. F. Hassan, Z. Guo, Z. Chen, H. Liu, *Mater. Res. Bull.* **2011**, *46*, 858.

[45] Y. Zhai, X. Ma, H. Mao, W. Shao, L. Xu, Y. He, Y. Qian, *Adv. Electron. Mater.* **2015**, *1*, 1400057.

[46] Y. Wang, W. Kang, P. Ma, D. Cao, D. Cao, Z. Kang, D. Sun, *Mater. Chem. Front.* **2020**, *4*, 1212.

[47] H. Kim, W. Choi, J. Yoon, J.H. Um, W. Lee, J. Kim, J. Cabana, W.-S. Yoon, *Chem. Rev.* **2020**, *120*, 6934.

[48] H. Nara, Y. Fukuhara, A. Takai, M. Komatsu, H. Mukaibo, Y. Yamauchi, T. Momma, K. Kuroda, T. Osaka, *Chem. Lett.* **2008**, *37*, 142.

[49] J. Lee, J. Moon, S. A. Han, J. Kim, V. Malgras, Y. Heo, H. Kim, S. Lee, H. K. Liu, S. X. Dou, Y. Yamauchi, M. Park, J. H. Kim, *ACS Nano* **2019**, *13*, 9607.

[50] X. Li, X. Sun, X. Hu, F. Fan, S. Cai, C. Zheng, G. D. Stucky, *Nano Energy* **2020**, *77*, 105143.

[51] B. Wang, J. Xue, F. Li, H. Geng, J. Lang, *ChemSusChem* **2021**, *14*, 5304.

[52] L. Yue, D. Wang, Z. Wu, W. Zhao, Y. Ren, L. Zhang, B. Zhong, N. Li, B. Tang, Q. Liu, Y. Luo, A. M. Asiri, X. Guo, X. Sun, *Chem. Eng. J.* **2022**, *433*, 134477.

[53] J. Yue, Q. Sun, Z. Fu, *Chem. Commun.* **2013**, *49*, 5868.

[54] Y. Xiao, X. Zhao, X. Wang, D. Su, S. Bai, W. Chen, S. Fang, L. Zhou, H. Cheng, F. Li, *Adv. Energy Mater.* **2020**, *10*, 200666.

[55] L. Shao, S. Wang, J. Qi, Z. Sun, X. Shi, Y. Shi, X. Lu, *Mater. Today Phys.* **2021**, *19*, 100422.

[56] Y. Fang, D. Luan, X. W. Lou, *Adv. Mater.* **2020**, *32*, 2002976.

[57] B. Peng, Z. Lv, S. Xu, J. Pan, W. Zhao, C. Dong, F. Huang, *Adv. Mater.* **2022**, 2200863.

[58] H. Kim, W. Choi, J. Yoon, J. H. Um, W. Lee, J. Kim, J. Cabana, W. Yoon, *Chem. Rev.* **2020**, *120*, 6934.

[59] R. Sun, S. Liu, Q. Wei, J. Sheng, S. Zhu, Q. An, L. Mai, *Small* **2017**, *13*, 1701744.

[60] Y. Zhang, J. Li, L. Ma, H. Li, X. Xu, X. Liu, T. Lu, L. Pan, *Chem. Eng. J.* **2022**, *427*, 130936.

[61] D. Su, M. Huang, J. Zhang, X. Guo, J. Chen, Y. Xue, A. Yuan, Q. Kong, *Nano Res.* **2020**, *13*, 2862.

[62] J. Li, N. Zhuang, J. Xie, X. Li, W. Zhuo, H. Wang, J. Na, X. Li, Y. Yamauchi, W. Mai, *Adv. Energy Mater.* **2020**, *10*, 1903455.

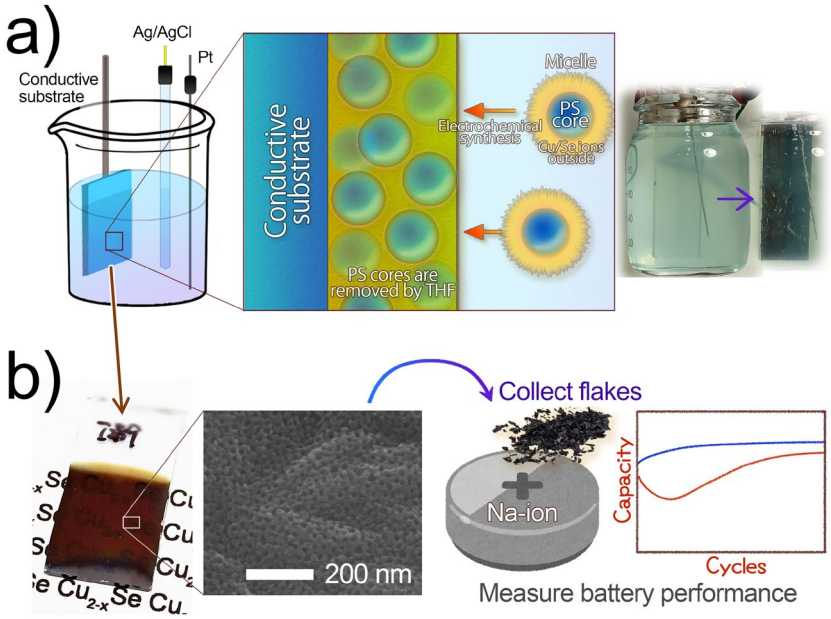

Figure 1. Schematic diagram illustrating (a) electrodeposition of mesoporous Cu_2Se and (b) sample photograph on an ITO substrate, surface FE-SEM image, and battery performance measurement.

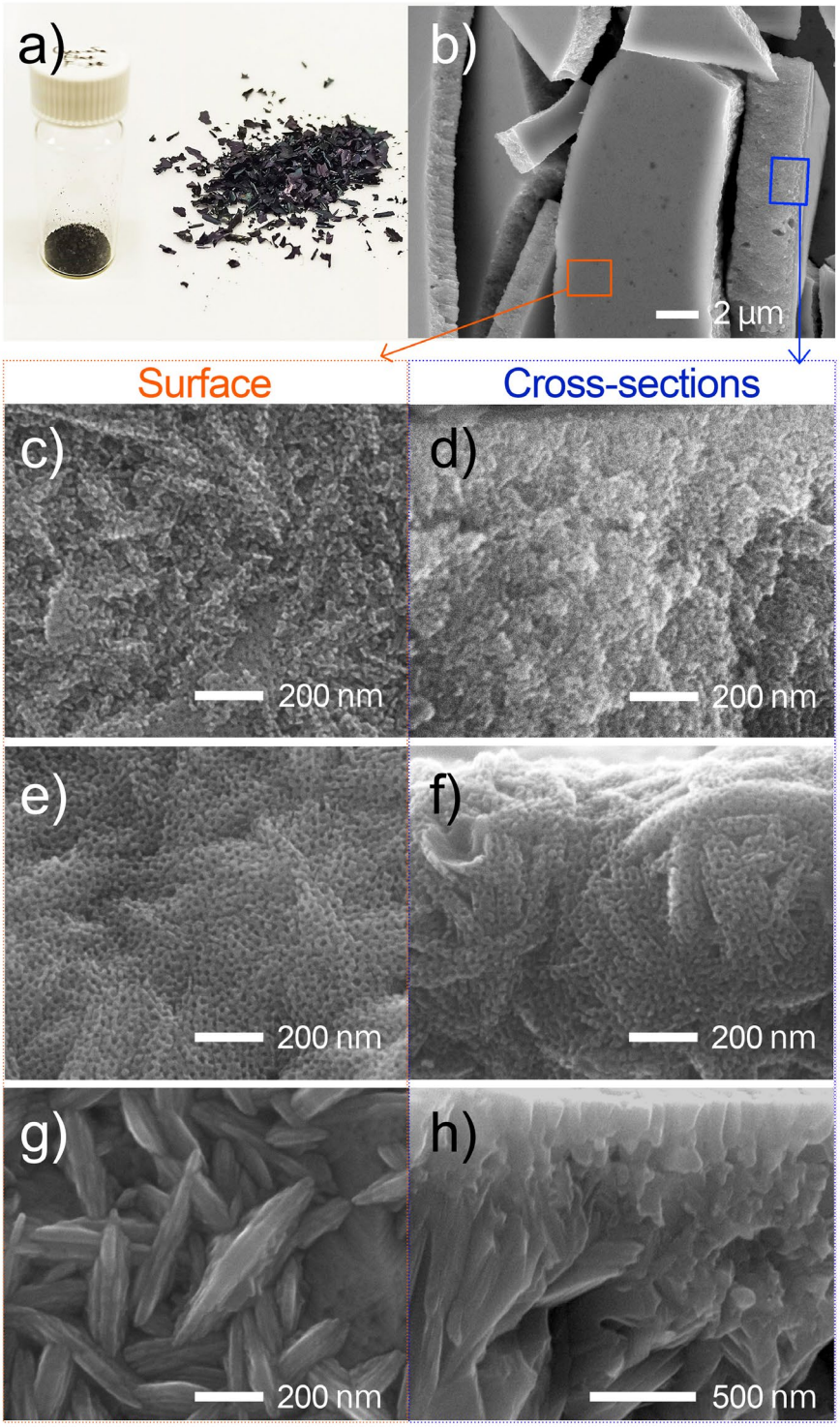

Figure 2. (a) Photograph of Cu_2Se flakes. (b) Low magnification SEM image of Cu_2Se flakes. FE-SEM images of Cu_2Se flakes: (c) their surface and (d) cross-sectional view of the 9-nm pore sample, (e) surface and (f) cross-sectional view of 18-nm pore sample, and (g) surface and (h) cross-sectional view of the non-porous sample.

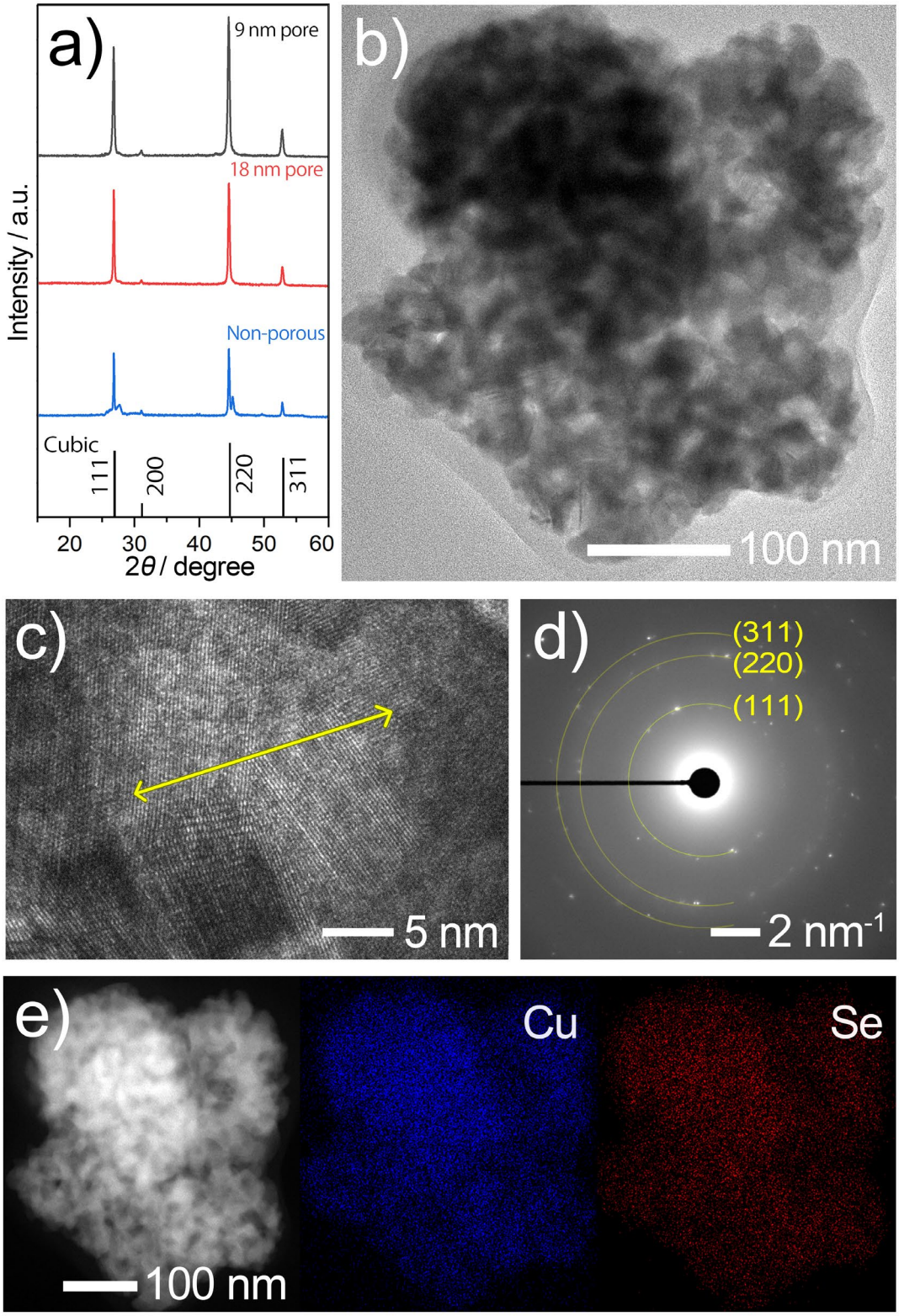

Figure 3. (a) XRD patterns for 9-nm pore, 18-nm pore, and non-porous samples. (b) TEM and (c) HRTEM images, (c) corresponding diffraction patterns taken from the selected area and (e) EDS elemental maps of the 18-nm pore sample.

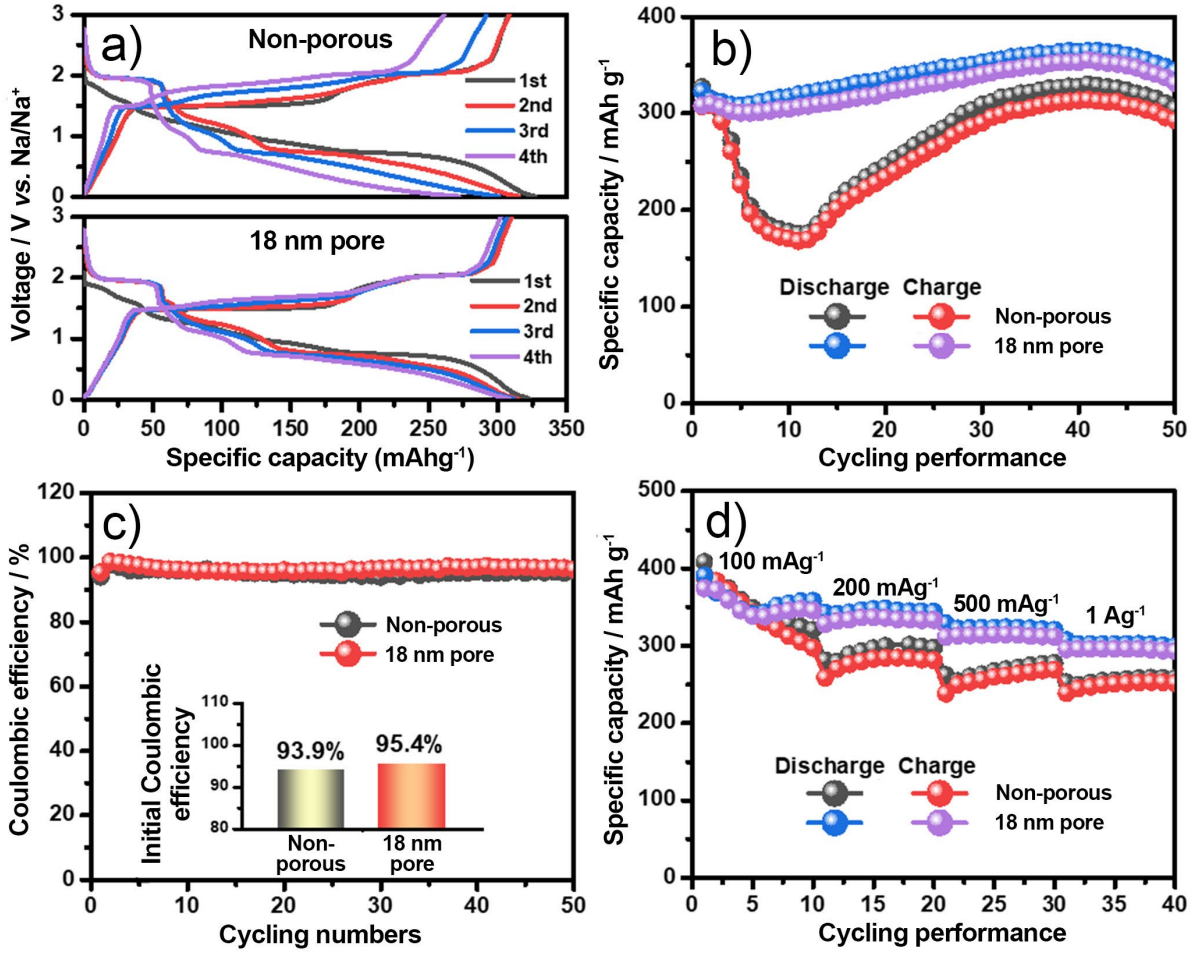

Figure 4. (a) Galvanostatic charge-discharge curves for non-porous and 18-nm pore samples. (b) Cycling performance, (c) Coulombic efficiencies and (d) rate performance of non-porous and 18-nm pore samples. The inset in Figure 4c shows the initial Coulombic efficiencies of non-porous and 18-nm pore samples.

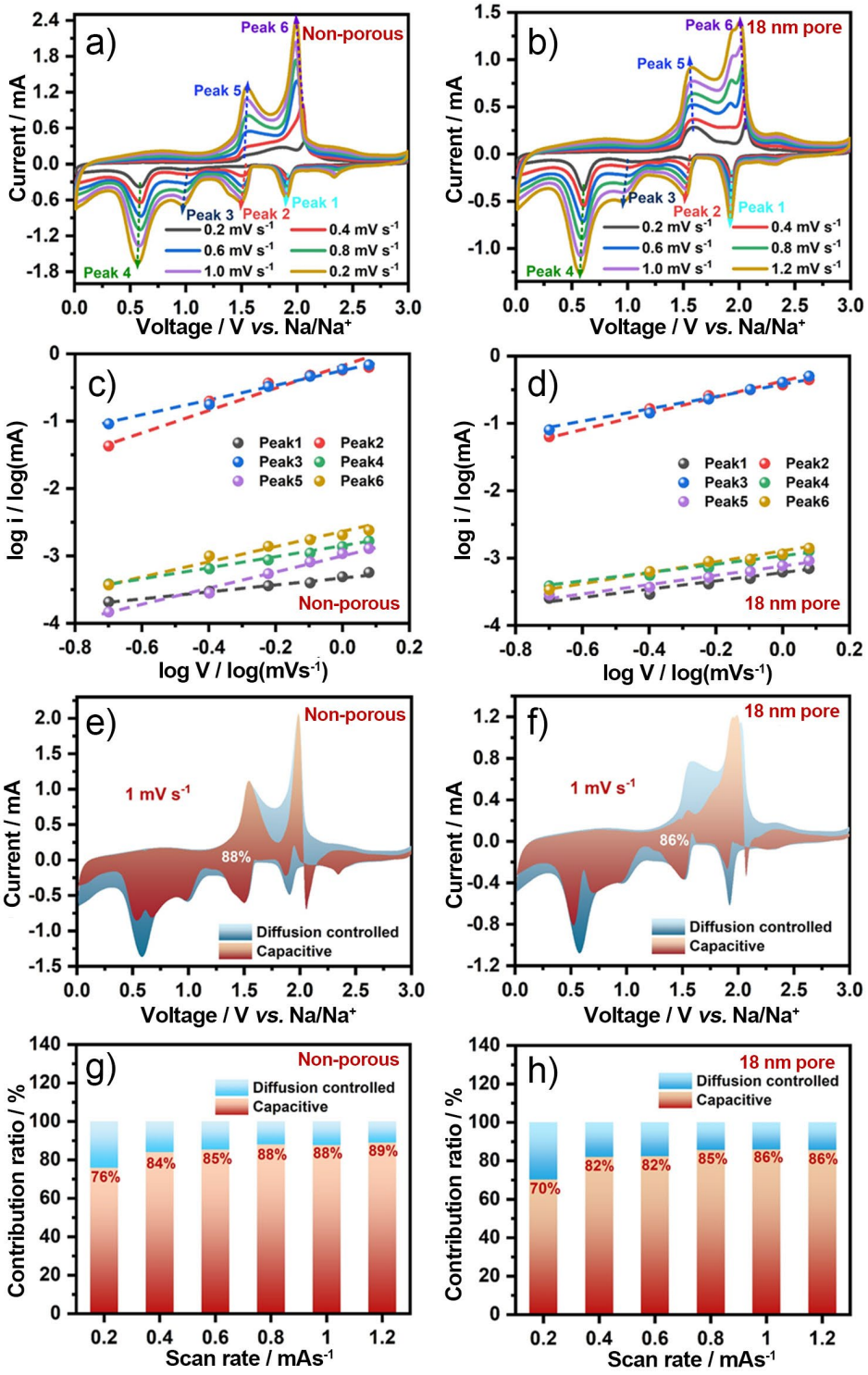

Figure 5. (a, b) CV curves of (a) non-porous and (b) 18-nm pore samples at different scan rates from 0.2 mV s^{-1} to 1.2 mV s^{-1}. (c, d) Relationship between log (i) and log (v) for (c) non-porous and (d) 18-nm pore samples. (e, f) Capacitive contribution region of (e) non-porous and (f) 18-nm pore samples at 1.0 mV s^{-1}. (g, h) Capacitive and diffusion-controlled behavior ratios of (g) non-porous and (h) 18-nm pore samples at different scan rates.

Abstract

The proposed synthesis method enables fabrication of mesoporous Cu_2Se flakes with huge electrochemically active surface area. Uniformly sized mesopores are homogeneously distributed within the flakes. The mesoporous electrode showshigh specific capacity (of more than 300 mAh g^{-1}),stable cycling performance and diffusion-controlled electrochemical behavior.

T. Nagaura, J. Li*, J. F. S. Fernande, A. Ashok, A. Alowasheeir, A. K. Nanjundan, D. V. Golberg, S. Lee, J. Na*, Y. Yamauchi*

Expeditious Electrochemical Synthesis of Mesoporous Chalcogenide Flakes: Mesoporous Cu_2Se as a Potential High-Rate Anode for Sodium-Ion Battery